



Confined local oxygen gas promotes electrochemical water oxidation to hydrogen peroxide

Xia, Chuan; Back, Seoin; Ringe, Stefan; Chen, Fanhong; Sun, Xiaoming; Siahrostami, Samira; Chan, Karen; Wang, Haotian

Published in:
Nature Catalysis

Link to article, DOI:
[10.1038/s41929-019-0402-8](https://doi.org/10.1038/s41929-019-0402-8)

Publication date:
2020

Document Version
Peer reviewed version

[Link back to DTU Orbit](#)

Citation (APA):
Xia, C., Back, S., Ringe, S., Chen, F., Sun, X., Siahrostami, S., Chan, K., & Wang, H. (2020). Confined local oxygen gas promotes electrochemical water oxidation to hydrogen peroxide. *Nature Catalysis*, 3, 125–134.
<https://doi.org/10.1038/s41929-019-0402-8>

General rights

Copyright and moral rights for the publications made accessible in the public portal are retained by the authors and/or other copyright owners and it is a condition of accessing publications that users recognise and abide by the legal requirements associated with these rights.

- Users may download and print one copy of any publication from the public portal for the purpose of private study or research.
- You may not further distribute the material or use it for any profit-making activity or commercial gain
- You may freely distribute the URL identifying the publication in the public portal

If you believe that this document breaches copyright please contact us providing details, and we will remove access to the work immediately and investigate your claim.

Confined local oxygen gas promotes electrochemical water oxidation to hydrogen peroxide

Chuan Xia^{a,b}† Seoin Back^c†, Stefan Ringe^c†, Kun Jiang^d, Fanhong Chen^e, Xiaoming Sun^e, Samira Siahrostami^{f,*}, Karen Chan^{g,*}, and Haotian Wang^{a,h*}

^a*Department of Chemical and Biomolecular Engineering, Rice University, Houston, TX 77005, United States*

^b*Smalley-Curl Institute, Rice University, Houston, TX 77005, United States*

^c*SUNCAT Center for Interface Science and Catalysis, Department of Chemical Engineering, Stanford University, Stanford, CA 94305, USA*

^d*School of Mechanical Engineering, Shanghai Jiaotong University, Shanghai 200240, China*

^e*State Key Laboratory of Chemical Resource Engineering, College of Energy, and Beijing Advanced Innovation Centre for Soft Matter Science and Engineering, Beijing University of Chemical Technology, 100029 Beijing, China*

^f*Department of Chemistry, University of Calgary, 2500 University Drive NW, Calgary, Alberta, Canada T2N 1N4*

^g*Department of Physics, Technical University of Denmark, Kongens Lyngby, Denmark 2800*

^h*Canadian Institute for Advanced Research, Toronto, Ontario M5G 1M1, Canada*

†contributed equally

*corresponding authors

E-mail: samira.siahrostami@ucalgary.ca; kchan@fysik.dtu.dk; htwang@rice.edu

Abstract

Electrochemical two-electron water oxidation is a promising route for renewable and on-site H₂O₂ generation as an alternative to the anthraquinone process. However, it is currently restricted by low selectivity due to strong competition from the traditional four-electron oxygen evolution reaction, as well as large overpotential and low production rates. Here we report an interfacial engineering approach, where by coating the catalyst with hydrophobic polymers we confine *in-situ* produced O₂ gas to tune the water oxidation reaction pathway. Using carbon catalysts as a model system, we show a significant increase of the intrinsic H₂O-to-H₂O₂ selectivity and activity compared to that of the pristine catalyst. The maximal H₂O₂ Faradaic efficiency was enhanced by 6-fold to 66% with an overpotential of 640 mV, under which H₂O₂ production rate of 23.4 μmol min⁻¹ cm⁻² (75.2 mA cm⁻² partial current) was achieved. This approach was successfully extended to nickel metal, demonstrating the wide applicability of our local gas confinement concept.

Hydrogen peroxide (H_2O_2) is one of the most important fundamental chemicals in modern chemical engineering industry as well as energy and environmental applications, with an annual global demand of about 4 million tons¹⁻⁶. It is currently produced through the energy-demanding and waste-intensive anthraquinone cycling process⁷, which is only economically viable on a relatively large scale and relies heavily on transportation and storage of unstable and hazardous bulk H_2O_2 solutions⁸. Using renewable electricity for on-site H_2O_2 generation *via* electrocatalytic processes has recently emerged as a promising alternative to traditional method⁹⁻¹⁴, with significant advantages including ambient reaction conditions, renewable energy source without fossil fuels, and green precursors such as water and air. As the oxidation state of oxygen (-1) in H_2O_2 sits between molecular oxygen and water, there are two possible ways for electrochemical H_2O_2 generation: One starts from O_2 *via* the two-electron oxygen reduction reaction (2e⁻-ORR); the other starts from H_2O *via* the 2e⁻ water oxidation reaction (2e⁻-WOR; $E^\circ = 1.76 \text{ V vs. normal hydrogen electrode; NHE}$)¹³. Both 2e⁻ pathways however compete with their otherwise 4e⁻ counterparts towards H_2O and O_2 respectively. While exciting progress has been made in developing highly selective catalysts for ORR towards H_2O_2 instead of H_2O ^{9-11,15,16}, there are very few known catalysts which can selectively and actively oxidize H_2O into H_2O_2 with stable performances^{12,13,17,18}. Most of reported water oxidation catalysts, such as metal oxides, hydroxides, chalcogenides, nitrides, and carbon materials, showed exclusive oxygen evolution reaction (OER) under water oxidation potentials¹⁹⁻²⁵. Steering the regular 4e⁻-WOR pathway towards the unconventional 2e⁻ pathway therefore becomes both fundamentally interesting for mechanistic understanding, and technologically important as a promising anode route for H_2O_2 generation. In addition, the development of high-

performance $2e^-$ -WOR catalysts, coupled with the corresponding $2e^-$ -ORR cathode catalysts, will enable an efficient H_2O_2 electrosynthetic cell where H_2O_2 can be selectively generated from both electrodes.

The key in tuning the WOR pathway relies on the interaction between catalytic surface and O intermediates, such as *O, *OH, and *OOH^{13,26}. In general, a proper interaction is desired for selective and active $2e^-$ -WOR: a too-strong OH binding could further oxidize *OH to *O and *OOH, finishing the complete $4e^-$ oxidation pathway towards O_2 ; a too-weak binding will lead to high kinetic barriers of water dissociation, dramatically slowing down the reaction rate¹³. Previous efforts have been focused on screening catalytic materials with proper electronic structures, such as wide band-gap metal oxides (ZnO , WO_3 , SnO_2 , TiO_2 , $BiVO_4$ and $CaSnO_3$)^{13,14,18,27}. While promising progress has been made in improving H_2O_2 selectivity, the state-of-the-art catalysts still present significant overpotentials of more than 1 V to deliver relatively low H_2O_2 partial currents ($\sim 10 \text{ mA cm}^{-2}$)^{13,14,18,27}. Unlike these materials' screening method for improving the performance of $2e^-$ -WOR, we propose to use locally generated O_2 gas, from the catalysts' surface, to effectively regulate the interaction with O intermediates and thus change the reaction selectivity and activity. Under a positive enough potential, most of the water oxidation catalysts will continuously evolve O_2 with their active sites refreshed after the generated O_2 gas bubbles away²⁸. We hypothesize that, if those generated O_2 gas can be confined around the active sites, the accumulated O_2 molecules could further interact with the catalysts' surface or the intermediate O species, and thus be able to tune the intermediate binding strength for completely different reaction pathways.

Here we report an interfacial engineering approach in which we trap *in-situ* produced O₂ gas close to active sites by coating the catalyst surface with hydrophobic polymers. Using OER-selective carbon catalysts as a model system, we observed a significant increase of the intrinsic H₂O-to-H₂O₂ selectivity and activity once generated O₂ gas was confined to the surface. The H₂O₂ selectivity was enhanced by 6-fold from only 11% on pristine carbon to a maximal of 66%. An impressive H₂O₂ production rate of 23.4 μmol min⁻¹ cm⁻² (75.2 mA cm⁻² partial current) was achieved under a small overpotential of 640 mV, which tops the performances reported in literature. With insights from *ab-initio* modeling, we postulate that the locally confined O₂ gas could shift the *OH binding on various carbon sites in the direction of improved H₂O₂ activity, through a decrease in solvation energies or a decrease in the *O coverage around catalytic sites. This local gas confinement approach was successfully extended to other OER-exclusive catalysts, such as nickel metal, for partial H₂O₂ generation, suggesting its wide applicability.

Results

Electrocatalytic 2e⁻-WOR. We first select a flat carbon surface to evaluate the relationship between O₂ gas confinement and H₂O₂ selectivity. Polytetrafluoroethylene (PTFE) polymer islands were deposited onto mirror-polished glassy carbon (GC) electrodes to artificially create an aerophilic surface in aqueous solutions (**Fig. 1a, Methods**)²⁹ using a shadow mask assisted spray-coated method. When a fixed positive potential higher than the onset of OER was applied, the PTFE islands can function as aerophilic centers around which the generated O₂ gas were confined to form gas-liquid-solid triple phase boundaries (**Fig. 1a**). Those locally confined O₂ bubbles may in turn interact with catalytic sites and

thus affect the H₂O₂ selectivity. With O₂ gas continuously produced, the bubbles will gradually grow and eventually leave the surface when the buoyant force becomes larger than the bubble adhesive force on the catalytic surface. Therefore, under steady-state O₂ evolution, the adhesive force of O₂ bubbles could represent the ability of the catalyst to confine local O₂ gas. By tuning the size of the PTFE patterning *via* a shadow mask-assisted spray coating method (**Supplementary Fig. 1, Methods**), we can change the adhesive force of O₂ bubbles on the GC surface and examine the resulting H₂O₂ selectivity.

A positive potential of 2.05 V versus the reversible hydrogen electrode (*vs.* RHE) was applied on three different samples as shown in **Fig. 1b-g**: pristine GC, GC with 300 μm (300-GC) and 200 μm (200-GC) PTFE patterning. While no obvious O₂ bubbles were observed on the surface of pristine GC, PTFE islands were able to accumulate the *in-situ* formed O₂ during water oxidation process³⁰ (**Fig. 1b** and **Supplementary Video 1-3**). This is consistent with the different adhesive forces on different surfaces. The pristine GC demonstrates a 21.3 μN adhesive force for O₂ bubble with an under-electrolyte bubble contact of $156.4^\circ \pm 1.6^\circ$ (**Fig. 1h**). In a sharp contrast, 300-GC and 200-GC offer a much stronger adhesive force of 80.7 and 106.0 μN , respectively, leading to stronger confinements of local gaseous O₂. Consistently, the under-electrolyte O₂ bubble contact angles of 300-GC and 200-GC (**inset of Fig. 1h**) decrease to $143.0^\circ \pm 0.8^\circ$ and $118.0^\circ \pm 2.1^\circ$, respectively, indicating the enhanced aerophilicity of the catalytic surfaces. The different local O₂ confinements result in different H₂O₂ activities and selectivity. The pristine GC presents an intrinsic H₂O₂ selectivity of 7.3% on carbon materials, which was gradually improved to 9.0% on 300-GC and further to 11.4% on 200-GC with similar trend to the adhesive force (**Fig. 1i**). This phenomenon reveals to us that the intrinsic H₂O₂

selectivity of carbon catalyst could be positively affected by the strength of local O₂ confinement.

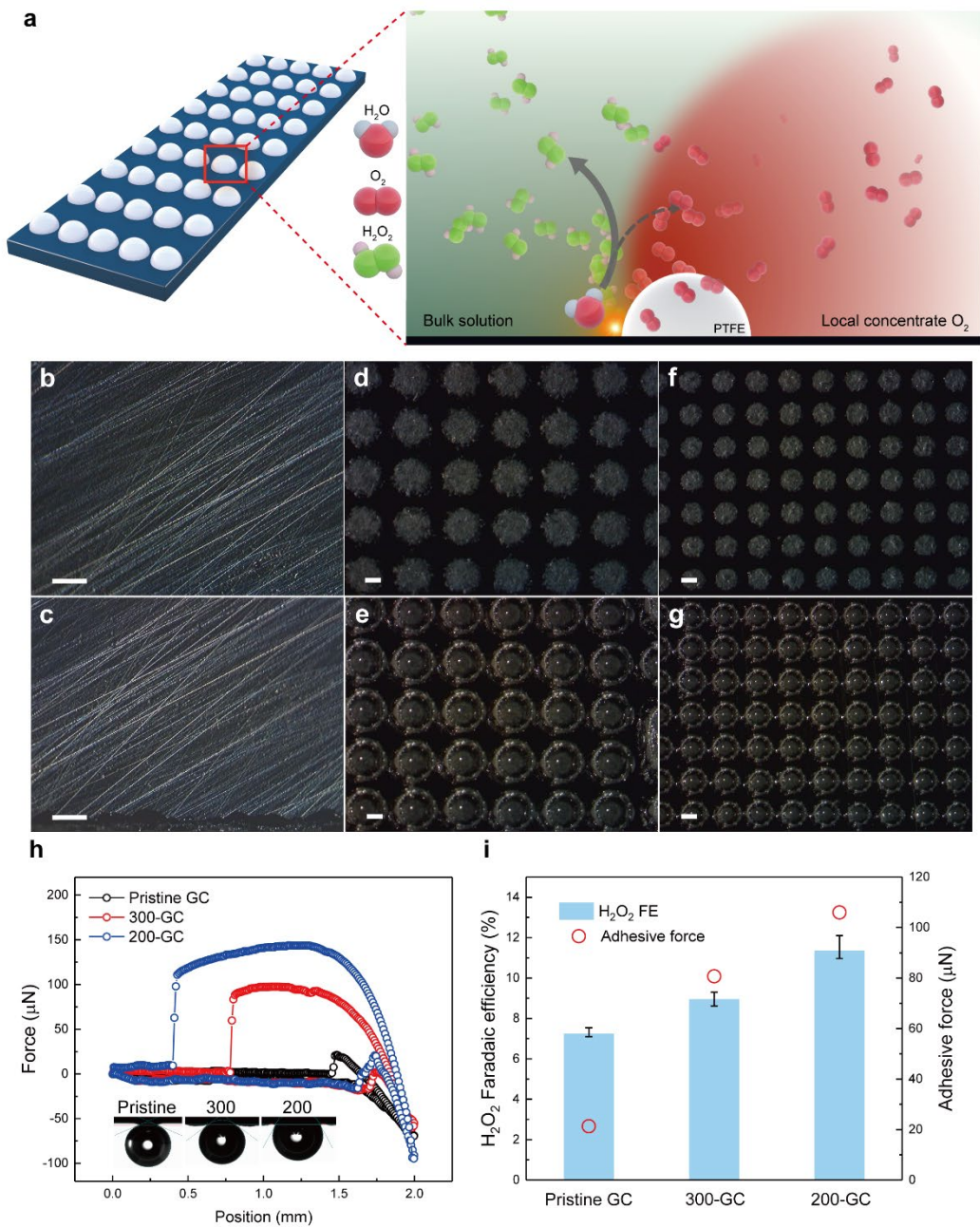


Fig. 1 | Experimental observation of local product concentration effect. **a**, A schematic showing the assumed possible reaction pathway tuning by local concentrate product. **b-g**, Digital photos for pristine and PTFE patterned GC in 1.0 M Na₂CO₃ electrolyte. **b-c**, pristine GC recorded at open circuit and 2.05 V vs. RHE, respectively. **d-e**, 300-GC recorded at open circuit and 2.05 V vs. RHE, respectively. **f-g**, 200-GC recorded at open

circuit and 2.05 V vs. RHE, respectively. It demonstrates that the pristine GC cannot hold any O₂ bubble on its surface, however, the PTFE patterned GC is able to concentrate the gaseous O₂ around the catalytic surface. Scale bars: **b-g** 300 μm. **h**, O₂ gas bubble adhesive force measurements for pristine GC, 300-GC and 200-GC electrode, demonstrating enhanced O₂ adhesive force of GC surface after PTFE loading. The insets show the O₂ bubble contact angles under electrolyte. **i**, The H₂O₂ Faradaic efficiency of pristine GC, 300-GC and 200-GC catalyst in 1.0 M Na₂CO₃ electrolyte at 2.05 V vs. RHE, where a monotonic increase of H₂O₂ FE was observed with increasing of O₂ bubble adhesive force. The applied potential of GC should be less than 2.1 V vs. RHE in order to prevent glassy carbon electrode damage by oxidation during long operation³¹. Thus, 2.05 V vs. RHE was chosen for water oxidation measurements. The error bars represent three independent samples.

To elaborate the possible reaction mechanisms and to further amplify the O₂ confinement effect for improved H₂O₂ generation performance, a systematic control of the loading of PTFE polymer coating on a three-dimensional porous carbon fiber paper (CFP) electrode was investigated. The polymer loading can be precisely controlled by changing the concentration of PTFE solution during the dip-coating process, where the 5% (CFP-5%), 20% (CFP-20%), and 60% (CFP-60%) PTFE solutions result in a PTFE mass loading (compared to that of CFP) of 12%, 55% and 150%, respectively (**Methods**). Scanning electron microscopy (SEM) analysis suggests that PTFE nanoflakes can be uniformly deposited on the surfaces of carbon fibers (**Supplementary Fig. 2a-b**), providing sufficient triple phase boundaries and gas confinement for two-electron water oxidation. As expected, the gas adhesive force gradually increased with increased PTFE coating, with consistently decreased under-electrolyte O₂ and increased in-air water contact angles (**Supplementary Fig. 3**), which we suggest to have a direct impact on the water oxidation catalytic activity and selectivity. First, since the PTFE coating repels water and leads to a lower electrochemical surface area (ECSA, **Supplementary Fig. 4**), the overall geometric current densities were gradually decreased compared to pristine CFP (**Fig. 2a**). However, the H₂O₂

selectivity showed a monotonic enhancement with increased PTFE coating (**Fig. 2b**). The peak H₂O₂ Faradaic efficiency (FE) of pristine CFP is *ca.* 10%, but increased to 23%, 31% and 66% by CFP-5%, CFP-20% and CFP-60% samples, respectively, which represents a maximal 6-fold enhancement in H₂O₂ selectivity (**Supplementary Fig. 5 and 6**). A similar trend was also observed in other electrolyte such as 1.0 M K₃PO₄ electrolyte (pH = 13.18; **Supplementary Fig. 7a**). We employed gas chromatography to quantify the FEs of gas products during water oxidation. Combining the gas chromatography and H₂O₂ titration results, we got an overall *ca.* 100% FE from H₂O-to-O₂ and H₂O-to-H₂O₂ processes (**Supplementary Fig. 7b**) with negligible CO or CO₂ from possible carbon oxidation (lower than the detection limit of the thermal conductivity detector), suggesting that the measured electrocatalytic anodic current exclusively stems from water oxidation reactions and the CFP is stable under our operation conditions. In addition, no obvious morphology evolution could be observed for PTFE modified CFP catalyst after electrochemical measurements (**Supplementary Fig. 2c-d**). The H₂O₂ evolution onset potential (defined as the potential where the H₂O₂ concentration reaches 1 ppm after 10 mins electrolysis) of CFP-60% sample was measured to be only 290 mV, which is among the best compared to previous catalysts.^{13,14} More importantly, in contrast to previous oxide catalysts which require large positive potentials (> 3 V vs. RHE) to deliver H₂O₂ current densities of *ca.* 10 mA cm⁻², the H₂O-to-H₂O₂ partial current on our CFP-60% catalyst ramps up quickly to 75.2 mA cm⁻² (23.4 μmol min⁻¹ cm⁻²) with a maximal 66% selectivity under only 2.4 V vs. RHE potential, which represents a record-high performance compared to existing catalysts (**Fig. 2c**).

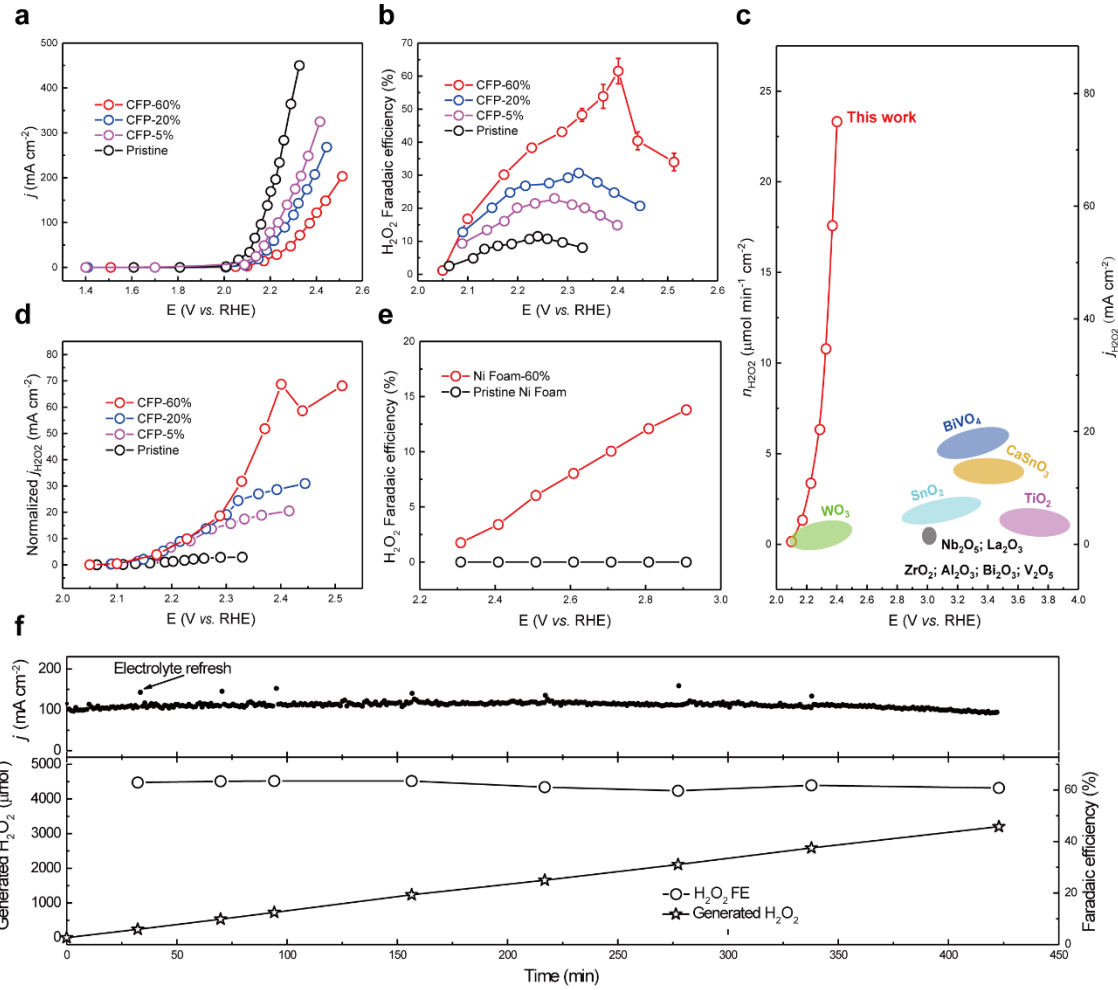


Fig. 2 | Water oxidation performances on CFP and Ni based catalysts in 1.0 M Na₂CO₃, pH 11.96. **a**, The overall current densities of the pristine CFP, CFP-5%, CFP-20% and CFP-60% catalysts. **b**, H₂O₂ Faradaic efficiencies on pristine CFP, CFP-5%, CFP-20% and CFP-60% at different applied potentials. The highest Faradaic efficiency reaches 66%. The error bars represent three independent samples. **c**, H₂O₂ generation rates of CFP-60% catalyst under different applied potential. The typically reported two-electron water oxidation catalysts, including BiVO₄, CaSnO₃, WO₃, SnO₂, TiO₂, Nb₂O₅, La₂O₃, ZrO₂, Al₂O₃, Bi₂O₃ and V₂O₅^{13,18,27}, are also listed for comparison. **d**, ECSA-normalized H₂O₂ production partial current density versus potential on pristine CFP, CFP-5%, CFP-20% and CFP-60%. **e**, H₂O₂ Faradaic efficiencies on pristine Ni foam and 60% PTFE solution modified Ni foam (Ni Foam-60%). Note that the potentials for Ni-based electrode are not *iR*-compensated. **f**, The overall current density and H₂O₂ Faradaic efficiency of CFP-60% catalyst at 2.4 V vs. RHE over the course of continuous electrolysis. The geometric area of the CFP-60% electrode is 0.36 cm².

We performed detailed experimental analysis to investigate the possible mechanism for this shift of the water oxidation pathway from 4e⁻ to 2e⁻. First, to exclude

possible contributions from O₂ plasma treatment, Argon annealing, or fluorine dopant during sample preparation processes, in one control we only treated the pristine CFP using O₂ plasma; in a second we annealed the pristine CFP at 350 °C; in a third we converted the CFP-60% sample into fluorine-doped carbon/CFP by high temperature annealing in Argon atmosphere (**Supplementary Fig. 2e-f**). The three control electrodes demonstrate similar two-electron water oxidation performance as pristine CFP, with a maximal H₂O₂ FE of 14.6%, 13.4% and 11.3%, respectively (**Supplementary Fig. 7c, d**). Secondly, to demonstrate that the carbon site selectivity for H₂O₂ formation is not related to the specific surface deposited materials, trimethoxy (1H,1H,2H,2H-heptadecafluorodecyl) silane was used to replace the PTFE to create the similar aerophilic surface to trap O₂ gas³² (**Supplementary Fig. 7e, f**). After silane modification, we found that the H₂O₂ selectivity of CFP can also be significantly boosted, demonstrating that the confined O₂ plays the role in promoting H₂O₂ selectivity. The above two pieces of evidence show that the carbon site selectivity is related neither to the fabrication processes nor the surface deposited materials, but could instead be directly linked to local O₂ concentration.

One may, at first glance, hypothesize that the locally confined O₂ gas shifts the H₂O-to-O₂ equilibrium towards its reverse reaction (O₂-to-H₂O), which potentially suppresses the 4e⁻ path and thus as a result increases H₂O₂ selectivity. However, this equilibrium factor can be ruled out by comparing the intrinsic activities of carbon sites with ECSA normalization (**Fig. 2d** and **Supplementary Fig. 4**): While 1) PTFE modified CFP catalysts presented higher H₂O₂ partial currents (more than an order of magnitude) compared to pristine CFP under different applied potentials, indicating their dramatically improved intrinsic H₂O-to-H₂O₂ catalytic activities; 2) the intrinsic H₂O-to-O₂ activity was

similar compared to pristine carbon (**Supplementary Fig. 8a**). Since the pressure/activity of locally confined O₂ gas does not directly impact the H₂O-to-H₂O₂ equilibrium, and on the other hand the 4e⁻ OER equilibrium was not obviously inhibited, we conclude that the enhanced H₂O₂ generation performances in our carbon catalyst systems are not due to the simple chemical equilibrium shift effect. We also note that the different PTFE-coated CFP samples showed quite similar H₂O₂ intrinsic activities within a certain potential window until they diverge at large overpotentials, where O₂ bubbles evolve violently, which further supports our hypothesis that increased confinement of O₂ gas at the interface has a positive correlation with H₂O₂ activity. Furthermore, similar H₂O-to-H₂O₂ performance was obtained using pristine CFP catalyst in Ar, Air and O₂ saturated electrolyte (**Supplementary Fig. 8b**), eliminating the possible contributions from dissolved O₂ in electrolyte. These results, taken together, suggest that the locally accumulated O₂ gas molecules may directly interact with carbon active sites or reaction intermediates, which as a result significantly shifts the water oxidation pathway from 4e⁻ of O₂ to 2e⁻ of H₂O₂.

We found that this concept of confining local O₂ gas to control the selectivity towards H₂O₂ can be successfully extended to other catalytic materials beyond carbon. As an example, we investigated Ni metal foam, which has been established as a highly active, OER-exclusive catalyst^{33,34}. As shown in **Fig. 2e**, we confirmed that while pristine Ni foam did not generate detectable H₂O₂, PTFE-coated Ni foam (**Methods**) achieves a H₂O₂ FE of 13.8% (20 mA cm⁻² H₂O₂ partial current) at an applied potential of 2.9 V vs. RHE, which has never been observed in Ni metal catalysts before.

Lastly, as performance stability is a common concern in previously reported H₂O-to-H₂O₂ catalysts due to their very high overpotentials³⁵, we performed

chronoamperometry on our CFP-60% catalyst by holding a 2.4 V *vs.* RHE potential where H_2O_2 selectivity is maximal (**Fig. 2f**). The current density showed negligible changes during the course of stability test. Around 61% H_2O_2 selectivity was still maintained after 7-hour continuous electrolysis, demonstrating the good stability of the catalyst over long operation period (**Supplementary Fig. 2c-d**). However, we should emphasize here that more works need to be done to extend the stability from the order of 10 hours to thousands of hours for future's possible application. This could be addressed by incorporating other catalytic materials with confined O_2 effects to further lower the overpotential for high-performance H_2O_2 generation.

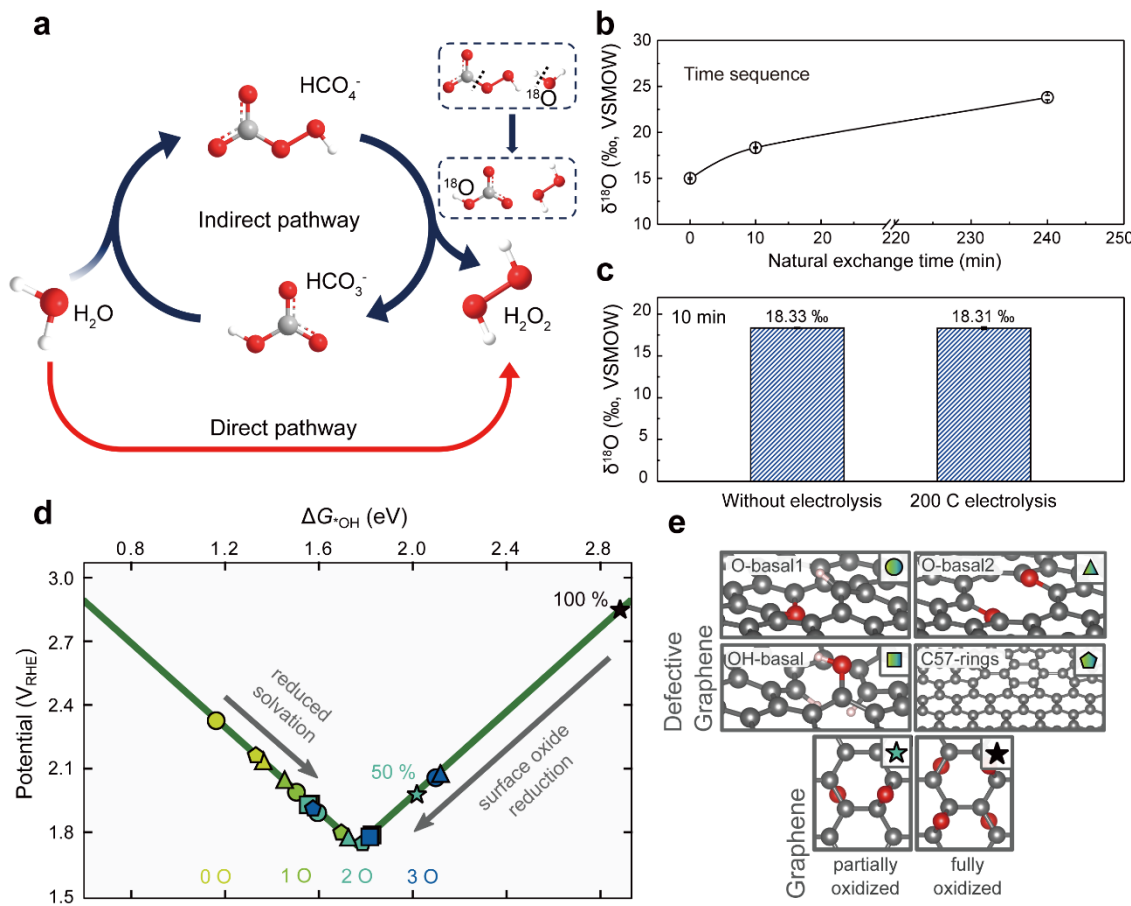


Fig. 3 | Possible mechanisms. **a**, Two different reaction pathways for catalytic two-electron water oxidation. **b**, ^{18}O isotope abundance in quickly dried (within 2 mins, Methods) 1.0 M Na_2CO_3 electrolyte with varied isotope exchange time between Na_2CO_3

solute and DI water. The analytical precision (1σ) is 0.05‰ for $\delta^{18}\text{O}$, and the values are reported as standard δ notation with respect to V-SMOW. **c**, ^{18}O isotope abundance in quickly dried 1.0 M Na_2CO_3 electrolyte with or without applied potential (2.4 V vs. RHE). The error bars in **b** and **c** represent two independent tests. **d**, 2e^- volcano plot of H_2O oxidation as a function of the $^*\text{OH}$ binding energy ($\Delta G_{^*\text{OH}}$). The data points depict $^*\text{OH}$ binding energies on defected graphene sheets (circles, pentagons, triangles and squares) as well as partially (50 %) and fully oxidized graphene sheets (stars) (without correction for solvation effects) and are schematically drawn in **e**. In case of the defected structures, four different typical defects were considered as well as different coverages of oxygen atoms in the vicinity of the active site indicated by yellow (low coverage, no $^*\text{O}$ in the vicinity, structures shown in panel **e**) to blue (high coverage, 3 $^*\text{O}$ in the vicinity) color scale. Arrows indicate potential external driving forces which likely influence the H_2O_2 selectivity by decreasing solvation stabilization due to the creation of water-poor oxygen bubbles or by reducing the degree of surface oxidation.

Proposed possible mechanisms. Previous two-electron water oxidation studies on oxides electrocatalysts suggested an indirect, percarbonate-involved mechanism (**Fig. 3a**).^{13,36,37} Firstly, the percarbonate species, such as HCO_4^- and $\text{C}_2\text{O}_6^{2-}$ are generated by electrochemical HCO_3^- oxidation on the electrode at a high applied potential. Subsequently, the percarbonate species are hydrolyzed by H_2O in the electrolyte, resulting in the formation of H_2O_2 and HCO_3^- . Based on this mechanism, a significant promotion effect on H_2O_2 formation was observed using bicarbonate electrolyte, *e.g.* KHCO_3 .^{13,36} However, in stark contrast to previous reports, the two-electron water oxidation performance of the CFP-60% catalyst is much better in 1.0 M Na_2CO_3 electrolyte compared with that in 1.0 M NaHCO_3 (**Supplementary Fig. 9**). No promotion effect could be observed using bicarbonate electrolyte in our case, indicating a different mechanism for our carbon catalyst systems. To further explore whether percarbonate intermediates are a possible reaction pathway, we performed oxygen isotope experiments. In our as-obtained Na_2CO_3 , the abundance of ^{18}O is different compared with that in DI water. The as-obtained Na_2CO_3 has a $\delta^{18}\text{O}$ of 14.99‰. As shown in **Fig. 3b**, after the fresh preparation of 1.0 M Na_2CO_3

solution, we observed a natural isotope oxygen exchange with increased $\delta^{18}\text{O}$ in Na_2CO_3 to 18.33‰ (10 min) and 23.79‰ (2 h). Therefore, within 10 mins during which the natural exchange does not reach equilibrium, if the percarbonate is the dominant reaction intermediates, we should be able to observe an ^{18}O isotope difference between the electrolyzed Na_2CO_3 and the bare one, considering the violent interaction and chemical bond reconfiguration between the HCO_4^- intermediate and H_2O (**Fig. 3a**). The isotope ratio mass spectrometry was employed to monitor the ^{18}O isotope in the samples, which offers an analytical precision (1σ) of 0.05‰ for $\delta^{18}\text{O}$ and the values are reported as standard δ notation with respect to V-SMOW (Methods)³⁸. After electrolysis with 200 C passing (~10 mins), 1 mL of the electrolyzed 1.0 M Na_2CO_3 solution was taken out, meanwhile another 1 mL of solution was taken from the unelectrolyzed bulk 1.0 M Na_2CO_3 solution. Then both of them were quickly dried in a surface dish at 100 °C. Of note, the natural exchange time with the DI water was same for the unelectrolyzed and electrolyzed Na_2CO_3 . As shown in **Fig. 3c**, the $\delta^{18}\text{O}$ value for 1.0 M Na_2CO_3 electrolyte with and without applied potential showed negligible change (18.31‰ vs. 18.33‰). This unchanged ^{18}O abundance in Na_2CO_3 after electrolysis implies that our catalyst systems do not follow the indirect mechanism. It is most likely that the electrocatalytic formation of H_2O_2 using our carbon catalysts follows the direct pathway (**Fig. 3a**).

The complexity of carbon materials together with the multi-scale nature of the here observed confined O_2 gas effect, makes it challenging to derive fully converged mechanistic explanations. Instead, we at this point present an *ab-initio* thermodynamic analysis of the complex interface and assess its qualitative contributions to the H_2O_2 product selectivity. We hope that these very initial discussions could involve

more detailed discussions in the future. Carbon materials including both GC and CFP are complex agglomerates of graphene-like structures, and give rise to a wide range of site motifs³⁹; the experimentally observed catalytic activity can therefore arise from a variety of active sites^{10,40}. For various water oxidation to H₂O₂ catalysts, theoretical onset potentials based on binding free energies of *OH (ΔG^{*OH}) have shown a good correlation with experiments, suggesting ΔG^{*OH} to be a meaningful descriptor¹³. In the present work, we thus consider the *OH binding energies at various coverages on four structures of defected graphene (O-basal 1, O-basal 2, OH-basal and 5555-6-7777 defective) which have been shown to weakly bind OH* and therefore are expected to be relevant active sites in the range of water oxidation to H₂O₂^{10,40}, as well as partially and fully oxidized graphene (**Methods, Supplementary Fig. 1e**).

Figure 3 shows the volcano plots for 2e⁻ water oxidation for the considered structures as a function of the ΔG^{*OH} . The active site models used in this work span a wide range of catalytic activities on both sides of the volcano. We postulate here that slight modulations of the *OH binding energy, arising from those trapped O₂ gas bubbles, can lead to significant improvements in H₂O₂ activity and selectivity. Two possible effects of the O₂ gas bubbles are as follows; firstly, the solvation stabilization may be decreased, since the presence of O₂ gas molecules interrupts hydrogen bonding networks and therefore reduces the average number of possible hydrogen bonds⁴¹. In aqueous solution, it has been experimentally and theoretically reported that adsorbed *OH is stabilized by 0.4 - 0.8 eV by hydrogen bonding interactions with nearby H₂O molecules⁴²⁻⁴⁴. By using a combination of explicit and implicit solvation approach⁴⁵, we found a solvation stabilization effect up of around 0.3 eV (**Supplementary Table 1**) which lies at the bottom

of the previously reported range. Although this value may vary depending on the surface and external conditions such as potential and pH, we generally expect the *OH binding to be weakened due to missing hydrogen bonding networks, which will shift the less oxidized defected active sites (yellow and light green symbols in **Fig. 3d**) towards the activity peak of the volcano plot.

Secondly, the reduced local H₂O concentration near the surface due to the trapped O₂ bubbles can lead to a decrease of the oxidation of the graphene surfaces, which in turn weakens *OH binding. This was confirmed by *operando* Raman spectroscopy that, under water oxidation reaction conditions the CFP-60% showed less oxidized surface than that of pristine CFP (**Supplementary Fig. 10**). The strong electrochemical driving force to generate *O coverage from H₂O, makes this process highly sensitive to the water chemical potential. On the other hand, O₂ chemical dissociation plays only a minor role even if large O₂ pressures are present inside the bubbles, due to the relatively small thermochemical driving force compared to water oxidation (**Supplementary Fig. 11**) and the high O₂ chemical dissociation barrier (> 2 eV)^{46,47}. It is thus the presence of H₂O molecules under the influence of a high electrochemical potential (2 - 3 V vs. RHE) which leads to a significant oxidization of the carbon material. Our surface Pourbaix analysis (**Supplementary Fig. 12 and 13**) of all structures shows that it is thermodynamically favorable to completely saturate the surface with oxygen. In the steady state, however, the surface might not be fully oxidized due to significant kinetic barriers for surface to subsurface O diffusion (> 4 eV)⁴⁸. This leads to free active sites where *OH can bind surrounded by a highly oxidized carbon environment. A high degree of oxidation localizes the *OH binding energy at the right, weak-binding leg of the volcano (**Fig. 3d**).

Consequently, a decrease in the H₂O concentration inside the O₂ bubbles and the corresponding decrease in surface oxidation would shift such sites to stronger *OH binding and higher H₂O₂ activity (**Supplementary Fig. 14**). Based on both the experimental and theoretical investigations, we conclude that the specific properties of the PTFE-CFP systems lead to less oxidized surfaces as well as water-poor regions in the created O₂ bubbles which could both shift the *OH binding energy of active sites to the top of the volcano thereby improving H₂O₂ activity, as summarized in the schematic diagram in **Supplementary Fig. 15**.

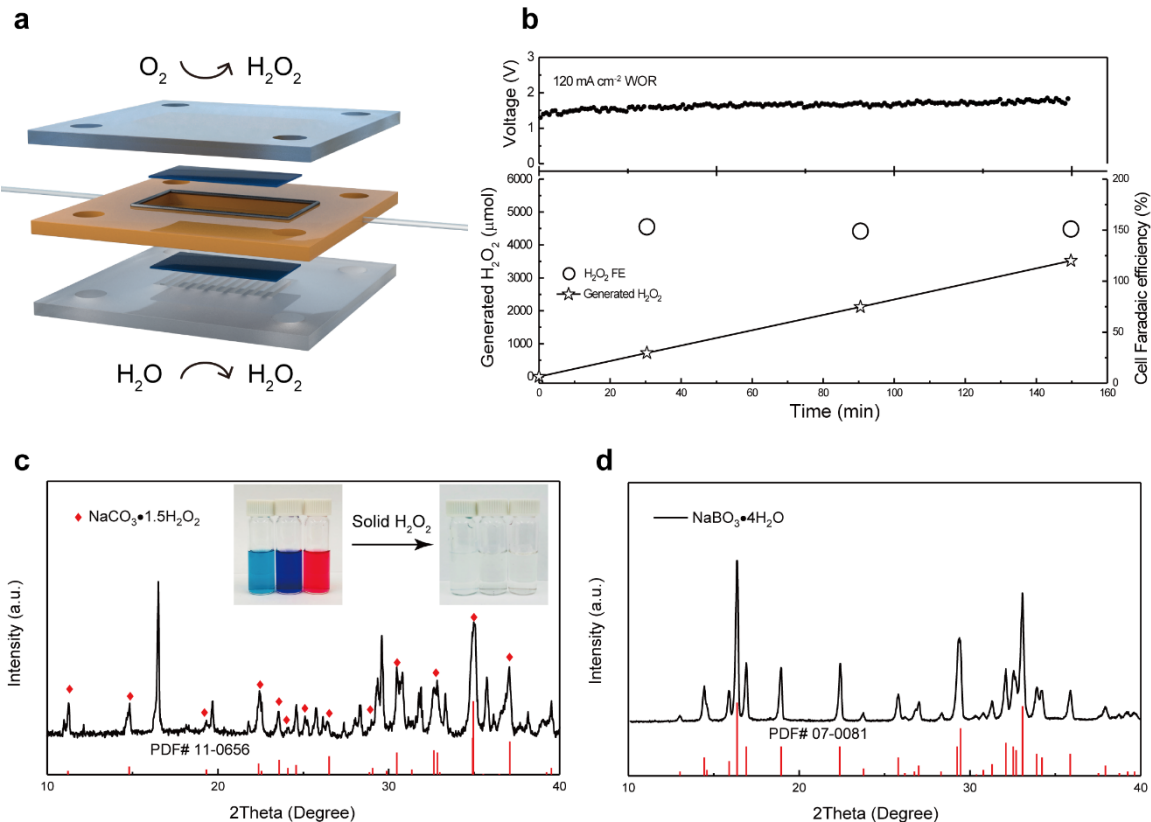


Fig. 4 | Applications of developed 2e⁻-WOR//2e⁻-ORR H₂O₂ electrosynthetic cell. **a**, schematic design of our H₂O₂ production prototype cell. **b**, H₂O₂ generation performance of our 2e⁻-ORR//2e⁻-WOR cell, which demonstrates an electricity-to-H₂O₂ efficiency of 90%, making it highly competitive to traditional anthraquinone oxidation technology. **c**, XRD pattern for as-extracted solid H₂O₂ from electrolyte after electrolysis (Na₂CO₃ + 1.5H₂O₂ → Na₂CO₃·1.5H₂O₂). The red rhombus symbol represents the peaks which originates from

$\text{Na}_2\text{CO}_3 \cdot 1.5\text{H}_2\text{O}_2$ (PDF no. 11-0656). All other peaks can be ascribed to hydrated Na_2CO_3 ($\text{Na}_2\text{CO}_3 \cdot \text{H}_2\text{O}$ and $\text{Na}_2\text{CO}_3 \cdot 7\text{H}_2\text{O}$). Inset of figure **c** shows the dye degradation using aged solid H_2O_2 which was stored under ambient conditions for two months, highlighting the stability and reliability of solid H_2O_2 compared to liquid H_2O_2 . The color image shows the pristine dye solution. The transparent one is the dye solution after reaction with solid H_2O_2 . **d**, XRD pattern for as-obtained sodium perborate ($\text{Na}_2\text{BO}_3 \cdot 4\text{H}_2\text{O}$), demonstrating the successful synthesis of pure high-value-added sodium perborate.

H_2O_2 electrosynthetic cell. This high-performance 2e^- -WOR catalyst, when coupled with an active and selective 2e^- -ORR cathode^{9,10}, can enable a highly efficient H_2O_2 electrosynthetic cell where H_2O_2 can be selectively generated from both electrodes. In contrast to previous 4e^- -WOR// 2e^- -ORR systems where the maximal H_2O_2 FE_{cell} was defined as 100%¹⁵, our 2e^- -WOR// 2e^- -ORR system can reach to a maximal H_2O_2 FE_{cell} of 200% (**Methods**), as two electrons shuttled from anode to cathode can maximally produce two H_2O_2 molecules. Here we demonstrate a membrane-free H_2O_2 electrocatalytic generation flow-cell with the state-of-the-art H_2O_2 generation rate and efficiency (**Fig. 4a, Methods**). Oxidized carbon nanotube¹⁰ was employed as an efficient and stable 2e^- -ORR catalyst (**Supplementary Fig. 16**) to couple with our CFP-60% anode. Only *ca.* 1.7 V_{cell} was required to reach a cell current of 50.4 mA (120 mA cm⁻² WOR) in our 2e^- -WOR// 2e^- -ORR cell (**Fig. 4b, Methods**), delivering a H_2O_2 FE_{cell} of 153%. This result agrees well with H_2O_2 selectivity on WOR (~ 60%) and ORR (~ 90%) catalysts when tested individually in standard three-electrode setup. An impressive H_2O_2 production rate of 24 $\mu\text{mol min}^{-1}$ was achieved in our electrosynthetic cell. This extraordinary current efficiency makes the electrochemical H_2O_2 synthesis cell highly competitive relative to energy-demanding anthraquinone cycling (**Supplementary Note 1**). This onsite H_2O_2 flow generation opens up opportunities in a wide range of practical applications⁴⁹, *e.g.* domestic

sewage treatment. We showed a representative demonstration here where by feeding the continuously produced H₂O₂ solution, the organic contamination in water can be rapidly degraded (**Supplementary Fig. 17a** and **Supplementary Video 4**). Furthermore, to minimize the transportation and storage cost of liquid H₂O₂, solid H₂O₂ powder — an adduct product between Na₂CO₃ and H₂O₂ (Na₂CO₃·1.5H₂O₂)⁵⁰ — was directly extracted from the Na₂CO₃ electrolyte after a continuous electrolysis (**Supplementary Fig. 17b, Methods**). Both X-ray diffraction (XRD) and XPS analysis (**Fig. 4c** and **Supplementary Fig. 18**) confirmed the successful preparation of solid H₂O₂, which is more stable and reliable than liquid H₂O₂.⁵⁰ We showed that the solid H₂O₂ powders were still highly active for organic dye degradation after two months storage under ambient conditions (**Fig. 4c** and **Supplementary Video 5**). Meanwhile, we demonstrated that other high-value products, *e.g.* sodium perborate (**Fig. 4d**), can be *in-situ* generated and precipitated out by simply adding sodium metaborate into the electrolyte.

Conclusions

Taken together, our experimental and theoretical results demonstrate the efficacy of our catalyst design concept, that accumulated local gaseous O₂ can shift the energetics of the water oxidation reaction in favor of 2e⁻ of H₂O₂ generation. Future studies will be directed towards more uniform and stable coating of hydrophobic materials to further boost the local O₂ concentration and prevent wetting after long-term operation. Additionally, our investigations on Ni suggest that higher activity and selectivity can be achieved by applying this concept on known H₂O-to-H₂O₂ catalysts. Fine characterizations on crystalline

catalysts will further allow computational simulations to study the mechanism and the origin of improvement in catalytic performances in detail.

References

- 1 Perry, S. C. *et al.* Electrochemical synthesis of hydrogen peroxide from water and oxygen. *Nature Reviews Chemistry*, **3**, 442-458 (2019).
- 2 Shen, R. *et al.* High-Concentration Single Atomic Pt Sites on Hollow CuSx for Selective O₂ Reduction to H₂O₂ in Acid Solution. *Chem* **5**, 2009-2110 (2019).
- 3 Campos-Martin, J. M., Blanco-Brieva, G. & Fierro, J. L. Hydrogen peroxide synthesis: an outlook beyond the anthraquinone process. *Angewandte Chemie International Edition* **45**, 6962-6984 (2006).
- 4 Kuttassery, F. *et al.* One Electron-Initiated Two-Electron Oxidation of Water by Aluminum Porphyrins with Earth's Most Abundant Metal. *Chemsuschem* **10**, 1909-1915 (2017).
- 5 Remello, S. N. *et al.* Two-electron oxidation of water to form hydrogen peroxide catalysed by silicon-porphyrins. *Sustainable Energy & Fuels* **2**, 1966-1973 (2018).
- 6 Mathew, S. *et al.* Two-Electron Oxidation of Water Through One-Photon Excitation of Aluminium Porphyrins: Molecular Mechanism and Detection of Key Intermediates. *ChemPhotoChem* **2**, 240-248 (2018).
- 7 Yang, S. *et al.* Toward the decentralized electrochemical production of H₂O₂: a focus on the catalysis. *ACS Catalysis* **8**, 4064-4081 (2018).
- 8 Edwards, J. K. & Hutchings, G. J. Palladium and gold-palladium catalysts for the direct synthesis of hydrogen peroxide. *Angewandte Chemie International Edition* **47**, 9192-9198 (2008).
- 9 Kim, H. W. *et al.* Efficient hydrogen peroxide generation using reduced graphene oxide-based oxygen reduction electrocatalysts. *Nature Catalysis* **1**, 282 (2018).
- 10 Lu, Z. *et al.* High-efficiency oxygen reduction to hydrogen peroxide catalysed by oxidized carbon materials. *Nature Catalysis* **1**, 156 (2018).
- 11 Siahrostami, S. *et al.* Enabling direct H₂O₂ production through rational electrocatalyst design. *Nature materials* **12**, 1137 (2013).
- 12 Izgorodin, A., Izgorodina, E. & MacFarlane, D. R. Low overpotential water oxidation to hydrogen peroxide on a MnO_x catalyst. *Energ Environ Sci* **5**, 9496-9501 (2012).
- 13 Shi, X. *et al.* Understanding activity trends in electrochemical water oxidation to form hydrogen peroxide. *Nat Commun* **8**, 701 (2017).
- 14 Kelly, S. *et al.* ZnO as an Active and Selective Catalyst for Electrochemical Water Oxidation to Hydrogen Peroxide. *ACS Catalysis* **9**, 4593–4599 (2019).
- 15 Han, L. *et al.* In-Plane Carbon Lattice-Defect Regulating Electrochemical Oxygen Reduction to Hydrogen Peroxide Production over Nitrogen-Doped Graphene. *ACS Catalysis* **9**, 1283-1288 (2019).

- 16 Zhao, K. *et al.* Enhanced H₂O₂ production by selective electrochemical reduction
of O₂ on fluorine-doped hierarchically porous carbon. *J Catal* **357**, 118-126 (2018).
- 17 Jiang, Y. *et al.* Selective Electrochemical H₂O₂ Production through Two-Electron
Oxygen Electrochemistry. *Adv Energy Mater* **8**, 1801909 (2018).
- 18 Fuku, K., Miyase, Y., Miseki, Y., Gunji, T. & Sayama, K. Enhanced oxidative
hydrogen peroxide production on conducting glass anodes modified with metal
oxides. *Chemistryselect* **1**, 5721-5726 (2016).
- 19 Kanan, M. W. & Nocera, D. G. In situ formation of an oxygen-evolving catalyst in
neutral water containing phosphate and Co²⁺. *Science* **321**, 1072-1075 (2008).
- 20 Finke, C. E. *et al.* Enhancing the activity of oxygen-evolution and chlorine-
evolution electrocatalysts by atomic layer deposition of TiO₂. *Energ Environ Sci*
12, 358-365 (2019).
- 21 Song, F. & Hu, X. Exfoliation of layered double hydroxides for enhanced oxygen
evolution catalysis. *Nat Commun* **5**, 4477 (2014).
- 22 Suntivich, J., May, K. J., Gasteiger, H. A., Goodenough, J. B. & Shao-Horn, Y. A
perovskite oxide optimized for oxygen evolution catalysis from molecular orbital
principles. *Science* **334**, 1383-1385 (2011).
- 23 McCrory, C. C., Jung, S., Peters, J. C. & Jaramillo, T. F. Benchmarking
heterogeneous electrocatalysts for the oxygen evolution reaction. *J Am Chem Soc*
135, 16977-16987 (2013).
- 24 Zhang, B. *et al.* Homogeneously dispersed multimetal oxygen-evolving catalysts.
Science **352**, 333-337 (2016).
- 25 Zheng, X. *et al.* Theory-driven design of high-valence metal sites for water
oxidation confirmed using in situ soft X-ray absorption. *Nat Chem* **10**, 149 (2018).
- 26 Viswanathan, V., Hansen, H. A. & Nørskov, J. K. Selective electrochemical
generation of hydrogen peroxide from water oxidation. *The journal of physical
chemistry letters* **6**, 4224-4228 (2015).
- 27 Park, S. Y. *et al.* CaSnO₃: An Electrocatalyst for Two-Electron Water Oxidation
Reaction to Form H₂O₂. *ACS Energy Letters* **4**, 352-357 (2018).
- 28 Xu, W., Lu, Z., Wan, P., Kuang, Y. & Sun, X. High-Performance Water
Electrolysis System with Double Nanostructured Superaerophobic Electrodes.
Small **12**, 2492-2498 (2016).
- 29 Lu, Z. *et al.* Superaerophilic carbon-nanotube-array electrode for high-performance
oxygen reduction reaction. *Advanced Materials* **28**, 7155-7161 (2016).
- 30 Yu, C., Zhang, P., Wang, J. & Jiang, L. Superwettability of Gas Bubbles and Its
Application: From Bioinspiration to Advanced Materials. *Advanced Materials* **29**,
1703053 (2017).
- 31 Kim, K.-W., Kuppuswamy, M. & Savinell, R. Electrochemical oxidation of
benzene at a glassy carbon electrode. *Journal of applied electrochemistry* **30**, 543-
549 (2000).
- 32 Lv, K. *et al.* Hydrophobic and Electronic Properties of the E-MoS₂ Nanosheets
Induced by FAS for the CO₂ Electroreduction to Syngas with a Wide Range of
CO/H₂ Ratios. *Advanced Functional Materials* **28**, 1802339 (2018).
- 33 Tang, C., Cheng, N., Pu, Z., Xing, W. & Sun, X. NiSe nanowire film supported on
nickel foam: an efficient and stable 3D bifunctional electrode for full water splitting.
Angewandte Chemie International Edition **54**, 9351-9355 (2015).

- 34 Wang, J., Zhong, H. x., Qin, Y. l. & Zhang, X. b. An Efficient Three-Dimensional
Oxygen Evolution Electrode. *Angewandte Chemie International Edition* **52**, 5248-
5253 (2013).
- 35 Park, S. Y. *et al.* CaSnO₃: An Electrocatalyst for 2-Electron Water Oxidation
Reaction to Form H₂O₂. *ACS Energy Letters* **4**, 352-357 (2018).
- 36 Fuku, K. & Sayama, K. Efficient oxidative hydrogen peroxide production and
accumulation in photoelectrochemical water splitting using a tungsten
trioxide/bismuth vanadate photoanode. *Chem Commun* **52**, 5406-5409 (2016).
- 37 Shi, X., Zhang, Y., Siahrostami, S. & Zheng, X. Light-Driven BiVO₄-C Fuel Cell
with Simultaneous Production of H₂O₂. *Adv Energy Mater* **8**, 1801158 (2018).
- 38 Coplen, T. B. Normalization of oxygen and hydrogen isotope data. *Chemical
Geology: Isotope Geoscience Section* **72**, 293-297 (1988).
- 39 Harris, P. Fullerene-related structure of commercial glassy carbons. *Philosophical
Magazine* **84**, 3159-3167 (2004).
- 40 Chen, S. *et al.* Defective Carbon-Based Materials for the Electrochemical Synthesis
of Hydrogen Peroxide. *ACS Sustainable Chemistry & Engineering* **6**, 311-317
(2017).
- 41 Siahrostami, S. & Vojvodic, A. Influence of adsorbed water on the oxygen
evolution reaction on oxides. *The Journal of Physical Chemistry C* **119**, 1032-1037
(2014).
- 42 Casalongue, H. S. *et al.* Direct observation of the oxygenated species during oxygen
reduction on a platinum fuel cell cathode. *Nature communications* **4**, 2817 (2013).
- 43 Karlberg, G. & Wahnström, G. Density-functional based modeling of the
intermediate in the water production reaction on Pt (111). *Physical review letters*
92, 136103 (2004).
- 44 Patel, A. M. *et al.* Theoretical Approaches to Describing the Oxygen Reduction
Reaction Activity of Single Atom Catalysts. *The Journal of Physical Chemistry C*
122, 29307-29318 (2018).
- 45 Mathew, K., Sundararaman, R., Letchworth-Weaver, K., Arias, T. & Hennig, R. G.
Implicit solvation model for density-functional study of nanocrystal surfaces and
reaction pathways. *The Journal of chemical physics* **140**, 084106 (2014).
- 46 Yan, H., Xu, B., Shi, S. & Ouyang, C. First-principles study of the oxygen
adsorption and dissociation on graphene and nitrogen doped graphene for Li-air
batteries. *Journal of Applied Physics* **112**, 104316 (2012).
- 47 Ni, S., Li, Z. & Yang, J. Oxygen molecule dissociation on carbon nanostructures
with different types of nitrogen doping. *Nanoscale* **4**, 1184-1189 (2012).
- 48 He, G., Liang, T., Wang, Q., Xu, M. & Liu, Y. Increased permeability of oxygen
atoms through graphene with ripples. *Soft matter* **13**, 3994-4000 (2017).
- 49 Yang, S. *et al.* Toward the decentralized electrochemical production of H₂O₂: a
focus on the catalysis. *ACS Catalysis* **8**, 4064-4081 (2018).
- 50 McKillop, A. & Sanderson, W. R. Sodium perborate and sodium percarbonate:
further applications in organic synthesis. *Journal of the Chemical Society, Perkin
Transactions* **1**, 471-476 (2000).
- 51 Jiang, K. *et al.* Transition-metal single atoms in a graphene shell as active centers
for highly efficient artificial photosynthesis. *Chem* **3**, 950-960 (2017).

- 52 Han, N. *et al.* Nitrogen-doped tungsten carbide nanoarray as an efficient bifunctional electrocatalyst for water splitting in acid. *Nat Commun* **9**, 924 (2018).
- 53 Kresse, G. & Joubert, D. From ultrasoft pseudopotentials to the projector augmented-wave method. *Physical Review B* **59**, 1758 (1999).
- 54 Kresse, G. & Furthmüller, J. Efficiency of ab-initio total energy calculations for metals and semiconductors using a plane-wave basis set. *Computational materials science* **6**, 15-50 (1996).
- 55 Wellendorff, J. *et al.* Density functionals for surface science: Exchange-correlation model development with Bayesian error estimation. *Physical Review B* **85**, 235149 (2012).
- 56 Blöchl, P. E. Projector augmented-wave method. *Physical review B* **50**, 17953 (1994).
- 57 Nørskov, J. K. *et al.* Origin of the overpotential for oxygen reduction at a fuel-cell cathode. *The Journal of Physical Chemistry B* **108**, 17886-17892 (2004).

Methods

Preparation of PTFE patterned glassy carbon. The shadow mask patterns are designed from CircuitMaster software. Polyimide substrate was pinned through a vacuum environment and LPFK Protolaser U3 ($f=103$ mm, $\lambda=355$ nm) was used to fabricate the polyimide shadow mask through direct laser engraving. Then, 1 mL of 60% polytetrafluoroethylene (PTFE) aqueous solution (Sigma) was spray-coated onto the glassy carbon (HTW GmbH) surface with the help of the polyimide shadow mask to obtain the well-defined PTFE patterns. After drying at 120 °C under ambient condition, the PTFE patterned glassy carbon samples were annealed at 350 °C under Argon atmosphere for 30 minutes to obtain a superaerophilic surface to accumulate the locally produced O₂.

Preparation of PTFE decorated CFP. 190 μm-thick CFP (Fuel Cell Store) was pre-treated by oxygen plasma (50 W, 2 minutes) to create a hydrophilic surface. Then, 2 × 5 cm² as-treated CFP was soaked into 60% (5% or 20%) PTFE aqueous solution for 10 minutes and then dried at 120 °C under ambient condition. Note that the 5% and 20% PTFE solutions are diluted from 60% PTFE. Next, the PTFE loaded CFP samples were annealed at 350 °C under Argon atmosphere for 30 minutes to obtain a superaerophilic surface to accumulate the locally produced O₂. The mass loadings of PTFE (mass different before and after surface modification) for CFP-5%, CFP-20% and CFP-60% are *ca.* 12%, 55% and 150%, respectively.

Preparation of FAS decorated CFP. 190 μm-thick CFP was pre-treated by oxygen plasma (50 W, 10 minutes) in order to introduce hydrophilic functional groups. Then, trimethoxy (1H,1H,2H,2H-heptadecafluorodecyl) silane (FAS) was used as the chemical vapor deposition material to increase the gas adhesive force of CFP, which was carried out in a beaker that contained FAS/ethanol solution (80 μL : 4 mL in volume) in equilibrium with its vapor. The plasma treated electrode was exposed to FAS vapor for 30 hr under ambient condition to receive aerophilic CFP-FAS electrode.

Preparation of control samples. O₂ plasma treated CFP sample was prepared by 50 W oxygen plasma functionalization for 2 minutes. The pristine CFP was calcined at 350 °C under Argon atmosphere for 30 minutes to obtain Argon annealed sample. The CFP-60% electrode was annealed at 900 °C under Argon atmosphere for 1 hr in order to fabricate the fluorine-doped carbon/CFP electrode.

Preparation of oxidized carbon material for oxygen reduction. The oxidized carbon nanotube was prepared according to previous report.¹⁰

Electrocatalytic oxidation of H₂O. The electrochemical measurements were run at 25 °C in a customized gastight H-type glass cell separated by Nafion 117 membrane (Fuel Cell Store). A BioLogic VMP3 workstation was employed to record the electrochemical response. In a typical three-electrode system, a platinum foil (Beantown Chemical, 99.99 %) and a saturated calomel electrode (SCE, CH Instruments) were used as the counter and reference electrode, respectively. The carbon electrodes (pristine and PTFE patterned glassy carbon; pristine and PTFE decorated CFP; ~ 1 cm²) were used as the working electrodes. The backside of glassy carbon was covered by an electrochemically inert, hydrophobic wax (Apiezon wax WW100) during electrochemical tests. Before electrochemical measurements, all samples were pre-stabilized at 1.2 V vs. SCE to achieve a stable current density in 1.0 M Na₂CO₃ electrolyte. All potentials measured against SCE was converted to the reversible hydrogen electrode (RHE) scale in this work using E_{RHE} = E_{SCE} + 0.244 V + 0.0591×pH, where pH values of electrolytes were determined by Orion 320 PerpHecT LogR Meter (Thermo Scientific). 1.0 M Na₂CO₃ aqueous solution was used as electrolyte in our study with pH of 11.96. Note that 4 mg mL⁻¹ Na₂SiO₃ (Sigma) was added into electrolyte to stabilize the formed H₂O₂ during stability measurements. The electrolyte in the anodic compartment was stirred at a rate of 1000 r.p.m. during electrolysis. Solution resistance (Rs) was determined by potentiostatic electrochemical impedance spectroscopy (PEIS) at frequencies ranging from 0.1 Hz to 200 kHz. All the measured potentials were manually compensated unless stated otherwise.

After electrolysis with 10 ~ 50 C passing, the generated H₂O₂ concentration was firstly roughly detected by using the standard H₂O₂ strips (Indigo Instruments), and further confirmed using standard potassium permanganate (0.1 N KMnO₄ solution, Sigma-Aldrich) titration process, according to following equation:



In this work, sulfuric acid (2.0 N H₂SO₄, VWR) was used as the H⁺ source. The Faradaic efficiency (FE) for H₂O₂ production is calculated using following equation:

$$\text{FE} = \frac{\text{generated H}_2\text{O}_2 \text{ (mol)} \times 2 \times 96485}{\text{total amount of charge passed (C)}} * 100 \text{ (maximum 100\%)} \quad (2)$$

In order to quantify the gas products during electrolysis, Argon gas (Airgas, 99.995 %) was delivered into the anodic compartment at a rate of 20.0 standard cubic centimeters per minute (sccm, monitored by Alicat Scientific mass flow controller) and vented into a gas chromatograph (Shimadzu gas chromatography-2014) equipped with a combination of molecular sieve 5 Å, Hayesep Q, Hayesep T, and Hayesep N columns. A thermal conductivity detector (TCD) was mainly used to quantify gas product concentration. The partial current density for produced O₂ was calculated as below:

$$j_i = x_i \times v \times \frac{n_i F p^0}{RT} \times (\text{electrode area})^{-1} \quad (3)$$

where x_i is the volume fraction of certain product determined by online gas chromatography referenced to calibration curves from the standard gas sample (Airgas), v is the flow rate of 20 sccm, n_i is the number of electrons involved, $p^0 = 101.3$ kPa, F is the Faradaic constant, $T = 298$ K and R is the gas constant. The corresponding Faradaic efficiency at each potential is calculated by $\frac{j_i}{j_{\text{overall}}} \times 100$.

For the 2e⁻-WOR//2e⁻-ORR electrosynthetic cell test, 0.5 mg cm⁻² oxidized carbon nanotube catalyst was air-brushed onto 2 cm² Sigracet 35 BC GDL (Fuel Cell Store) electrodes as 2e⁻-ORR cathode. And, 0.42 cm² CFP-60% electrode was used as anode. The two electrodes were therefore placed into opposite sides in the flow-cell⁵¹ without separation membrane. O₂ saturated 1.0 M Na₂CO₃ with 4 mg mL⁻¹ Na₂SiO₃ was used as electrolyte. The cathode was open to the atmosphere. The flow rate of 1.0 M Na₂CO₃ electrolyte was 5 mL min⁻¹ controlled by a peristaltic pump. A current of 50.4 mA was employed for H₂O₂ production. To extract the solid H₂O₂ from the electrolyte after electrolysis (three-electrode configuration, 25 mL 1.0 M Na₂CO₃ electrolyte, electrolysis at 2.4 V vs. RHE at 5 °C for 5 days; the CFP-60% catalyst was replaced using fresh catalyst after every 24 h; Bipolar membrane was used to replace the Nafion 117; the cathode was coupled with two-electron ORR using oxidized carbon nanotube electrode), about 100 mL of absolute ethanol is added into 20 mL of the electrolyte, and the mixture is mechanically stirred. The precipitate is isolated by vacuum filtration and washed several times with absolute ethanol. The isolated precipitate is then dried in a vacuum oven at room temperature for 24 h. For sodium perborate synthesis, a solution contains of 2.0 M NaBO₂ and 1.0 M Na₂CO₃ was used as electrolyte. And the electrolysis was performed at a current density of 120 mA cm⁻² at 5 °C. The *in-situ* formed white precipitate (sodium perborate) during electrolysis was collected for further characterizations.

The Faradaic efficiency of the electrosynthetic cell for H₂O₂ production and the corresponding electricity-to-H₂O₂ efficiency are calculated using following equations, respectively:

$$\text{FE}_{\text{cell}} = \frac{\text{generated H}_2\text{O}_2 \text{ (mol)} \times 2 \times 96485}{\text{total amount of charge passed (C)}} * 100 \text{ (maximum 200\%)} \quad (4)$$

$$\text{Electricity to H}_2\text{O}_2 \text{ efficiency} = \frac{E_{2e-\text{WOR}} - E_{2e-\text{ORR}}}{E_{\text{cell}}} * \text{FE}_{\text{cell}} \text{ (maximum 200\%)} \quad (5)$$

where $E_{2e-\text{WOR}}$ (1.76 V)¹³ and $E_{2e-\text{ORR}}$ (0.76 V)¹¹ are the theoretical potential for two-electron water oxidation and two-electron oxygen reduction, respectively. E_{cell} is the required cell voltage to offer a current density of 120 mA cm⁻².

Characterization. Powder X-ray diffraction data were collected using a Bruker D2 Phaser diffractometer in parallel beam geometry employing Cu K α radiation ($\lambda = 1.54056\text{\AA}$) and a 1-dimensional LYNXEYE detector, at a scan speed of 0.02° per step and a holding time of 1 s per step. X-ray photoelectron spectroscopy was obtained with a Thermo Scientific K-Alpha ESCA spectrometer, using a monochromatic Al K α radiation (1486.6 eV) and a

low energy flood gun as neutralizer. All XPS spectra were calibrated by shifting the detected carbon C 1s peak to 284.6 eV. SEM was performed on a Zeiss Supra55VP field emission scanning electron microscope with in-lens detector. The contact angles of O₂ gas bubbles under electrolyte were tested by the method of captive bubble⁵² and the bubble size was controlled at 2 μ L. Adhesive forces between the O₂ bubbles and electrodes were assessed using Dataphysics DCAT21.

¹⁸O isotope measurement. Firstly, 0.2 mol (21.2 g) Na₂CO₃ (Sigma) was dissolved into 200 mL ultrapure Milli-Q water. After stirring for 5 mins, 25 mL of the fresh 1.0 M Na₂CO₃ solution was used as electrolyte for water oxidation. After electrolysis with 200 C passing, 1 mL of the electrolyzed 1.0 M Na₂CO₃ solution was taken out, meanwhile another 1 mL of solution was taken from the unelectrolyzed bulk 1.0 M Na₂CO₃ solution. Then both of them were quickly dried (within 2 mins) in a surface dish at 100 °C. Of note, the natural exchange time with the water was same for the unelectrolyzed and electrolyzed Na₂CO₃. Next, the dried Na₂CO₃ powder was collected for ¹⁸O isotope analysis. Oxygen isotope analysis is performed on a Gas Bench-Conflo-Isotope Ratio Mass Spec (Delta V, ThermoScientific) system. ~0.190 mg Sodium carbonate (Na₂CO₃) were weighed out into an exetainer, then was flushed by Helium flow for 10 minutes on Gas Bench. 0.3 ml 105% phosphoric acid was added into the exetainer for 24 hour reaction. The generated CO₂ gas was then delivered to mass spectrometry for isotope ratio analysis. Oxygen isotope composition of carbonate are calculated based on measured oxygen isotope composition of CO₂ gas, based on the fractionation factor between the two at reaction temperature. Oxygen isotope values are reported in a delta notation, with respect to international standard, Vienna Standard Mean Ocean Water (VSMOW).

Operando Raman measurement. For *operando* electrochemical Raman spectroscopy measurements, a piece of carbon fiber paper (1 cm², with or without PTFE treatment) was first stuck onto a polished glassy carbon electrode via a conductive carbon tape and then assembled into a homemade three electrode spectroelectrochemical cell. The Raman spectra were recorded on a Horiba LabRAM HR 800 confocal Raman microscopy, with the signals excited by a 532-nm Ventus VIS laser and collected by a 100x objective, at a dispersion grating of 600 g mm⁻¹ and a co-adding of 64 scans. A Biological VSP potentiostat was used for potential control.

ECSA measurement. The ECSA was determined by measuring the capacitive current associated with double-layer charging from the scan-rate dependence of cyclic voltammetry (CV). Before ECSA measurements, all samples were pre-stabilized at 1.2 V *vs.* SCE to achieve a stable current density in 1.0 M Na₂CO₃ electrolyte. By plotting the difference in current density (j) between anodic and cathodic sweeps (Δj) at a fixed potential against the scan rate, a linear trend is observed. The fitting slope is twice of the double-layer capacitance (C_{dl}), which is linearly promotional to the ECSA. These values of C_{dl} permit comparison of relative surface activity of different electrodes particularly in same electrolyte. To determine C_{dl} for various electrodes, the potential window of CVs was 0.15 - 0.25 V *vs.* SCE with the scan rates from 50 mV s⁻¹ to 150 mV s⁻¹. Based on our previous work⁵¹, the double-layer capacitance of flat glassy carbon electrode is measured to be *ca.* 24 μ F cm⁻². Thus, the value of 24 μ F cm⁻² was used here for ECSA normalization.

Computational methods. Density functional theory (DFT) calculations were performed using the Vienna Ab Initio Simulation Package (VASP)^{53,54} with BEEF-vdW exchange-correlation functional⁵⁵ and projector augmented-wave (PAW) pseudopotential⁵⁶. The energy cutoff, a convergence criterion for self-consistent iteration and geometry relaxation were set to 500 eV, 10^{-4} eV and 0.05 eV/Å, respectively. To simulate various carbon structures with a wide range of catalytic activities, we modelled four different structures (O-basal 1, O-basal 2, OH-basal and 5555-6-7777 defective) using (6×6) graphene, which have been shown to be active for H₂O oxidation^{10,40}. Additionally, we considered partially and fully oxidized graphene using (1×2) graphene. We added 15 Å of vacuum layer to avoid non-physical interactions between repeating layers in z-direction. For large cells, a gamma point mesh was used, while for small oxidized graphene cells, $(6 \times 5 \times 1)$ meshes were used, which showed a negligible difference compared to $(12 \times 10 \times 1)$ meshes calculations. To test the effect of the implicit solvation, we used VASPsol with default parameter settings and a dielectric constant set to that of water ($\epsilon = 78.4$)⁴⁵.

At high applied overpotentials, the strongly oxidizing reaction conditions lead to carbon atoms being covered by adsorbed oxygen significantly affecting the catalytic properties. We therefore calculated binding free energies of *O (ΔG^*_{O}) on top and below the graphene sheet at different oxidation states referenced to free energies of H₂ and H₂O gas phase molecules. To investigate the effect of surface adsorbed *O on catalytic activity, we calculated *O coverage-dependent *OH binding free energies (ΔG^*_{OH}), which is a key intermediate in electrochemical H₂O oxidation to H₂O₂¹³.

To convert calculated electronic energies into free energies, we added free energy corrections for adsorbates which include zero-point energy, enthalpy and entropy at 300 K using the harmonic oscillator approximation. For gaseous molecules, we used the ideal gas approximation with the partial pressure of 101,325 Pa for H₂, and 3,534 Pa for H₂O, which is the vapor pressure of H₂O. The effect of potential was included using the computational hydrogen electrode (CHE) method⁵⁷, where the chemical potential of proton and electron pair equals to that of a half of hydrogen gas ($\mu(H^+ + e^-) = 1/2 \mu(H_2)$) at standard conditions. As the potential is applied, the chemical potential of an electron is shifted by $-eU_{\text{elec}}$, where e and U_{elec} are elementary charge and electrode potential, respectively.

Data availability

The data that support the plots within this paper and other findings of this study are available from the corresponding authors upon reasonable request.

Competing interests

All authors declare that they have no competing interests.

Acknowledgements

This work was supported by Rice University. H.W. is a CIFAR Azrieli Global Scholar in the Bio-inspired Solar Energy Program. C.X. acknowledges support from a J. Evans Attwell-Welch Postdoctoral Fellowship provided by the Smalley-Curl Institute. This work was performed in part at the Shared Equipment Authority (SEA) at Rice University. The authors acknowledge Lei Fan for the design of the scheme in Fig. 3. The authors also acknowledge Dr. Qiu Jiang, Dr. Tao Sun and Dr. Zhiyi Lu for their support to the experiment and useful discussions. K.C. acknowledges a grant (9455) from VILLUM FONDEN, and S.R. acknowledges funding from U.S. Department of Energy, Office of Science, Office of Basic Energy Sciences, Chemical Sciences, Geosciences, and Biosciences Division, Catalysis Science Program to the SUNCAT Center for Interface Science and Catalysis.

Author contributions

C.X. and H.W. conceptualized the project. H.W., K.C., and S.S. supervised the project. C.X. synthesized the catalysts. C.X. conducted the catalytic tests and the related data processing. C.X. performed materials characterization and analysis with the help of K.J., F.C. and X.S.. S.B. and S.R. performed the theoretical study. C.X. and H.W. wrote the manuscript with support from all authors.